AIAA JOURNAL
Vol. 38, No. 2, February 2000

Traveling Instability Waves in a Mach 8 Flow over an Elliptic Cone

Jonathan Poggie* and Roger L. Kimmel†
U.S. Air Force Research Laboratory, Wright–Patterson Air Force Base, Ohio 45433-7521
and
Stephen N. Schwoerke‡
Lockheed Martin Corporation, Fort Worth, Texas 76101-0748

Simultaneous measurements were carried out with three hot-film probes in the Mach 8 flow over an elliptic cone of 2:1 aspect ratio, and the data obtained were compared to the results of computations using the parabolized Navier–Stokes equations and linear stability theory. The elliptic-cone flow was found to be significantly different from the flows studied in previous hypersonic-flow stability experiments, which have focused exclusively on wind-tunnel models with two-dimensional, planar or axial symmetry. At least two instability mechanisms appear to be active in the present flow: one associated with the region of maximum crossflow in the vicinity of the shoulder of the cone and the other associated with the inflectional velocity profiles on the top centerline. Between the shoulder and leading edge of the cone, the dominant flow instability occurred at relatively low frequency, and the direction of the phase velocity was significantly skewed from that of the boundary-layer-edge streamlines. The results were found to be in rough agreement with linear stability calculations and are suggestive of a traveling crossflow instability mode, which apparently has not been observed before in hypersonic flow. The flow in the vicinity of the top centerline of the cone was found to be highly unstable and appeared in the experiments to be transitional. For this region of the flow, both the experiments and the computations showed an unstable frequency band that coincided with the characteristic second-mode frequency. The present experimental technique was adequate to identify the two instabilities present in the flow, but additional work will be required to achieve a detailed validation of linear stability computations for this configuration.

Nomenclature

c_r	= phase speed
$E[\,]$	= expectation value
f	= frequency
G	= one-sided autospectrum
h	= enthalpy
$\Im$	= imaginary part of complex number
L	= length of elliptic cone, 1.016 m
l_ξ, l_η	= axial and circumferential probe separations
Ma	= Mach number
N	= natural logarithm of disturbance amplitude ratio
$\Re$	= real part of complex number
R	= hot-film probe resistance
Re_x	= Reynolds number, $U_\infty x/\nu_\infty$
S	= cross-spectrum
s	= hot-film signal
T	= temperature or signal record duration
t	= time
U	= streamwise velocity component
x, y, z	= axial, spanwise, and vertical coordinates (Fig. 1)
γ^2	= coherence derived from cross spectrum
δ	= boundary-layer thickness (based on $h_0/h_{0_\infty} = 1.0008$ in this study)
θ	= angle in cylindrical coordinate system (Fig. 1)
λ	= wavelength
ν	= kinematic viscosity
ξ, η	= axial and circumferential coordinates in tangent plane
τ	= time delay between detection at each sensor
ϕ	= phase of cross spectrum
Ψ	= angle between phase velocity and axial direction

Subscripts

DS	= downstream probe
e	= boundary-layer-edge conditions
LAT	= lateral probe
US	= upstream probe
w	= wall conditions
0	= stagnation conditions
∞	= freestream conditions (upstream of shock)

Superscripts

$*$	= complex conjugate
$\hat{}$	= Fourier transform

Introduction

MUCH of the past work on hypersonic boundary-layer stability has focused on flows over bodies with two-dimensional, planar or axial symmetry. The instability mechanisms are now fairly well understood for this class of flows. If, in the reference frame of a neutral wave, part of the boundary-layer profile is supersonic, then multiple modes exist.[1,2] The modes are distinguished by their characteristic functions or profiles along the wall-normal direction. The first mode is often described as vortical in nature, whereas the second and higher modes have an acoustic character. In the hypersonic flow regime the first two modes are typically dominant, and both are essentially inviscid instabilities.[3] The direction of propagation of the most unstable first-mode wave is skewed from the freestream direction, whereas the second mode is unskewed. The second mode has a characteristic wavelength of about 2δ and a characteristic frequency of approximately $U_e/(2\delta)$.

Linear stability computations[4,5] have indicated that instability waves in three-dimensional hypersonic boundary layers display

Presented as Paper 98-0435 at the AIAA 36th Aerospace Sciences Meeting, Reno, NV, 12–15 January 1998; received 19 May 1998; revision received 3 March 1999; accepted for publication 22 June 1999.

*Research Aerospace Engineer, Air Vehicles Directorate, AFRL/VAAC, 2210 Eighth Street. Senior Member AIAA.

†Research Aerospace Engineer, Air Vehicles Directorate, AFRL/VAAA, 2130 Eighth Street, Suite 1. Senior Member AIAA.

‡Engineering Specialist, Mail Zone 2275, P.O. Box 748, Tactical Aircraft Systems.

several unique features. Both first- and second-mode waves may be skewed from the outer flow. A new class of inviscid instability may appear, driven by an inflection point in the profile of the velocity component perpendicular to the flow direction at the boundary-layer edge (crossflow). The character of crossflow instability is well-established for subsonic and moderately supersonic flows.[6] Corotating vortices form with their axes aligned approximately with the streamwise direction. The spanwise wavelength is on the order of the boundary-layer thickness, and the wave-number vector is typically oriented at large angle to the inviscid-flow streamlines. Stability calculations indicate that the most amplified disturbances are typically traveling waves, but experimental results are often dominated by roughness-induced stationary disturbances.

There are two extant experimental studies of the stability of three-dimensional hypersonic boundary layers, both involving sharp cones of circular cross section at an angle of attack: a test of a 7-deg half-angle cone at Mach 7.9 in a conventional wind-tunnel facility[7] and a flared-cone experiment at Mach 5.9 in a quiet wind tunnel.[8] Both experiments focused on the windward and leeward rays of the cone; no data were obtained along lateral rays.

Despite the different test articles and wind-tunnel environments, the overall results of the two studies were substantially similar. Both studies detected the presence of a second-mode instability as a peak in the hot-wire power spectrum at the characteristic frequency $U_e/(2\delta)$. For the 7-deg circular cone the flow along the windward ray was more stable and along the leeward ray less stable than the flow over the same model at zero incidence; a similar trend was seen with the flared cone. It is difficult to determine whether a crossflow instability was present in these experiments because the measurements were limited by facility noise and instrumentation sensitivity, particularly for the flow along the leeward ray, where the thick boundary layer drove the characteristic instability frequencies down into the range of the facility noise. (A small peak of frequency higher than the characteristic second-mode frequency was observed in hot-wire spectra obtained on the leeward ray of the flared cone,[8] but this result is difficult to interpret in the absence of corresponding linear stability computations.)

A different approach was adopted for the present study, which investigated stability and transition on a fully three-dimensional test article. Hot-film probe measurements were made in a Mach 8 flow over an elliptic cone of 2:1 aspect ratio, a case designed to induce a basic-state flow susceptible to crossflow instability. The design study for these experiments[9] and the mean flow features[10] have been reported previously. The focus of this component of the study was to identify the instability modes present in the flow and compare their properties (such as wavelength and phase velocity) to predictions from linear stability computations.

Methods

The experiments were conducted in the von Kármán Gas Dynamics Facility Tunnel B at the Arnold Engineering Development Center. The tests were carried out under adiabatic wall conditions at a measured freestream Mach number of $Ma_\infty = 7.93$ and a stagnation temperature of $T_0 = 728$ K in the settling chamber.

The freestream flow in Tunnel B has been extensively monitored and calibrated.[11] The mean Mach number on the tunnel centerline is spatially uniform to within 1.2%. The broadband rms mass flux (the disturbance level) on the centerline is between 1.2 and 1.5% of the local mean, depending on the unit Reynolds number. RMS total-temperature fluctuations are an order of magnitude smaller. The freestream disturbance spectrum is similar for all unit Reynolds numbers for both mass-flux and total-temperature fluctuations. It peaks at frequency of $f = 2$–3 kHz and drops off for higher frequencies as approximately $1/f$.

The experimental model was a sharp-nosed (40-μm spherical radius) cone with a 2:1 elliptical cross section and a half-angle of 7 deg in the minor axis (Fig. 1). Additional details of the experimental model and test conditions are reported in a companion paper.[10]

Hot-Film Probe Measurements

The hot-film measurements were made with custom-built probes operated in constant-current mode. The time-series data from the probes were used primarily to determine the coherence and phase of the cross spectra, which are independent of the calibration and frequency response of the hot-film anemometry system. Thus (for convenience) we were able to neglect probe calibration and to use an anemometer amplifier designed for hot-wire probes. The characteristic roll off caused by thermal-lag attenuation for a hot-wire sensor is 6 dB per octave, but only 3 dB per octave for a hot-film sensor. Because the anemometer amplifier was designed to compensate for the hot-wire roll off, there is a mismatch in anemometer compensation, and some quantitative distortion of the autospectra (but not of the cross spectra) is expected.

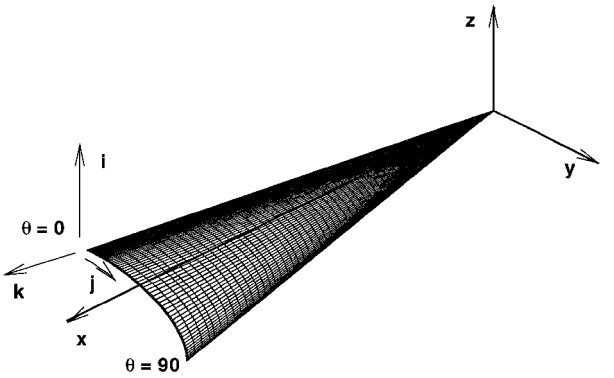

Fig. 1 Geometry and coordinate system of elliptic-cone model. See also Fig. 1 of Ref. 10.

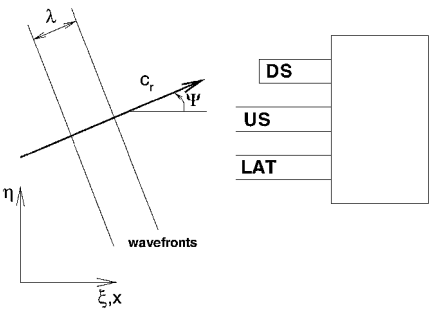

Fig. 2 Diagram of hot-film probe array. Reference frame is a plane tangent to the cone surface. See also Fig. 1 of Ref. 10.

The relative sensitivity of hot-film probes to total-temperature and mass-flux fluctuations depends on the local flow conditions and on the overheat ratio. All measurements were made at the maximum hot-film overheat attainable without risking film burnout. Because of the high stagnation temperature at Mach 8, this overheat ratio $R/R_0 - 1$ was considerably less than one. The separate mass-flux and total-temperature components of the hot-film signal could not be computed because insufficient data were obtained, but past work under similar flow conditions has shown that the raw anemometer output at these relatively low overheat ratios reflects primarily total-temperature fluctuations.[12] In the absence of probe calibration, the absolute magnitude of the signal spectra cannot be compared from station to station because the probe sensitivity changes with changing local mean flow conditions.

Flowfield surveys were made using a retractable overhead drive mechanism housed in an airlock immediately above the top of the wind-tunnel test section. This mechanism traversed in a direction approximately normal to the model surface: 10.4 deg from the vertical, halfway between the major- and minor-axis half-angles. The probe system on the overhead drive consisted of a probe foot with three hot-film probes with a lateral spacing of 3.18 mm (shown schematically in Fig. 2). Two probes (designated LAT and US) were positioned at the same x location to measure lateral time delay, and one probe (designated DS) was positioned 3.18 mm downstream to measure streamwise time delay.

Measurements at different circumferential locations were made by rolling the model, rolling the probe foot to orient the probe tips tangent to the model surface, and traversing the boundary layer to the location where the maximum broadband rms signal

was recorded. The majority of the measurements were made at $x/L = 0.8$ at roll angles between the top centerline ($\theta = 0$ deg) and the leading edge ($\theta = 90$ deg). The data were taken under adiabatic wall conditions (as determined by wall-temperature measurements) at a freestream (upstream of the shock) unit Reynolds number of $U_\infty / \nu_\infty = 1.97 \times 10^6$ m^{-1} for a local Reynolds number of $Re_x = 1.6 \times 10^6$. Some additional data were obtained at $x/L = 0.47$ ($Re_x = 0.93 \times 10^6$), but a poor signal-to-noise ratio at this streamwise station allowed useful data to be obtained at only one circumferential station ($\theta = 45$ deg).

Three channels of data were obtained simultaneously, band-pass filtered between 10 Hz and 500 kHz, and recorded using a Bell and Howell Model VR3700B analog tape recorder. The data were later digitized from the FM tape using a CAMAC (computer-automated measurement and control) data acquisition system from Kinetic Systems, Inc., and stored on a Pentium PC for analysis. Software for controlling the CAMAC system was written by the authors. For convenience, the tape was replayed at half speed and sampled at 500 kHz to give an effective sampling rate of 1.0 MHz. Three channels of data were digitized simultaneously in records of 2^{21} contiguous samples per channel. (These relatively long record lengths were selected so that convergence of the spectral statistics could be studied for different window sizes.)

At each measurement station a run at zero hot-film overheat was carried out to assess the noise level in the measurement system. The spectrum below about 100 kHz was relatively unaffected by noise, but a broad noise spectrum peaking around 350 kHz contaminated the higher-frequency range. Under the assumption that the noise is uncorrelated with the signal, it is permissible to subtract the measured noise spectrum from the measured data spectrum to give an improved estimate of the signal spectrum.[13] This procedure was carried out for the autospectra and cross spectra. The high-frequency noise was eliminated from the data, and little apparent effect was seen in the data for frequencies below 100 kHz.

Similar measurements with multiple hot-film probes have been made of the two-dimensional flow over a circular cone in the same wind-tunnel facility, and detailed consideration has been given to both systematic and random errors in cross spectra derived from the data.[14] Random error in the cross spectrum, which is inversely proportional to the square root of the number of records averaged, should be relatively small for the large data sets considered here. Systematic error caused by bias in the electronics of the anemometer system has been examined[14] and determined to induce a phase difference between channels of no more than 2 deg. It is difficult to quantify the possible systematic error caused by the interaction of the probes with the flowfield, and this issue needs to be addressed in future work.

Signal Analysis

Signal analysis was carried out in the frequency domain. Both the autospectra based on the signal from a single hot-film probe and cross spectra based on the signals from a pair of probes were computed. Software for analyzing the data was written by the authors; the signal analysis algorithms were adapted from standard texts.[13,15]

If the signal from a probe is denoted $s(t)$ and its Fourier transform is $\hat{s}(f)$, then the one-sided autospectrum of a random signal is defined as

$$G(f) = 2 \lim_{T \to \infty} (1/T) E[|\hat{s}(f, T)|^2] \tag{1}$$

where $E[\,]$ denotes the expectation-value operator over an ensemble of experiments, approximated here by a mean value over a set of signal records. The dependence of the finite Fourier transforms of the sample records on the record length T is indicated explicitly. Note that both the expectation operation and limit operation are required with random data to obtain a consistent estimator of the spectrum. This contrasts with the case of periodic data, where it is sufficient to take only the limit. Both the autospectra and the cross spectra (discussed next) were processed digitally in windows of 1024 points, tapered with the Hanning window function to suppress side-lobe leakage and averaged with 50% overlap for a total of 4095 blocks of data per channel. Tests with windows of different sizes (up to 16,384 points) showed no significant changes in the results.

The cross spectrum of a pair of signals $s_1(t)$ and $s_2(t)$ is defined in a similar manner:

$$S_{12}(f) = \lim_{T \to \infty} (1/T) E[\hat{s}_1^*(f, T) \hat{s}_2(f, T)] \tag{2}$$

where $*$ indicates a complex conjugate. Because the cross spectrum is, in general, a complex quantity, it is usually more convenient to work with measures of its amplitude and phase. One measure of the amplitude is the coherence, defined as

$$\gamma^2(f) = \frac{|S_{12}(f)|^2}{S_{11}(f) S_{22}(f)} \tag{3}$$

The coherence can be thought of as a frequency-dependent cross correlation of the signal. The phase angle is defined as

$$\phi(f) = \arctan \left\{ \frac{\Im[S_{12}(f)]}{\Re[S_{12}(f)]} \right\} \tag{4}$$

The phase function is related to the time delay between the two signals as follows:

$$\tau(f) = \phi(f)/2\pi f \tag{5}$$

A constant time delay produces a phase function that is a linear function of the frequency.

Measurements of the wavelength, speed, and propagation direction of disturbances in the boundary layer can be used to identify the instability modes present in the flow. Such measurements are not straightforward in three-dimensional flow because of the unknown direction of wave propagation. One procedure that has been used in studies of three-dimensional incompressible boundary layers is to use a pair of sensors on a rotating mount and attempt to zero the time delay between sensors.[16,17] Rotating the probe array was not considered to be feasible for the present study, and so a related approach, based on analysis of the signals from the fixed array of three hot-film probes, was adopted.

Keeping in mind that the phase velocity (the speed of a constant phase surface normal to itself) does not obey the ordinary rules of vector addition, we note that the following geometric relationship holds for a quasi-planar wave intercepted by a pair of point probes lying in the ξ–η plane tangent to the cone's surface (see Fig. 2):

$$c_r \tau = l_\eta \sin \Psi + l_\xi \cos \Psi \tag{6}$$

The probe separations l_ξ and l_η are known for each pair of hot-film probes, and time delay τ between sensors can be computed from Eq. (5). Thus, a pair of simultaneous equations for c_r and Ψ can be solved for any set of two pairs of probes. With the two pairs of probes labeled 1 and 2, the equation for the wave angle is

$$\Psi = \arctan \left[\frac{\tau_2 l_{\xi 1} - \tau_1 l_{\xi 2}}{\tau_1 l_{\eta 2} - \tau_2 l_{\eta 1}} \right] \tag{7}$$

and the phase speed can be found from

$$c_r = (l_{\eta 1} \sin \Psi + l_{\xi 1} \cos \Psi)/\tau_1 \tag{8}$$

The angle Ψ is measured from the ξ axis, which is the projection of the x axis (axial direction) onto a plane tangent to the cone's surface (see Fig. 2) and is positive for angles outboard of the top centerline of the cone.

Computational Procedures

A detailed discussion of the computational modeling of this configuration, including grid-resolution studies, was presented in an earlier paper.[9] For brevity, only a short summary of the computational procedure is given here.

The basic state computations for the laminar boundary-layer flow were carried out using the UPS PNS code, as modified by Lockheed Martin Tactical Aircraft Systems.[18] The code uses a second-order, central-difference scheme for inviscid fluxes and a fourth-order smoothing model. The outer boundary condition was a shock-fitting

model, and the solution for the first 25 mm of the cone was obtained with a Navier–Stokes nose solution code. The computational grid for the nose solution consisted of 121 × 71 × 31 points, and the PNS grid was 121 × 71 × 875 points, for both cases distributed over one 90-deg quadrant of the cone along the radial, circumferential, and axial directions, respectively (see Fig. 1). The basic state computations agreed, within the experimental uncertainty, with the measured wall pressure and heat flux in the region where laminar flow prevailed in the experiment.[10]

The e^{Malik} code[19] was used for the linear stability calculations. The version of the code used in this study did not include coordinate-system curvature terms for the elliptic cone. Nevertheless, a rough agreement between the results of the linear stability computations and the experimental data was observed. (Details are presented next.) The linear stability computations were intended to serve as a guide in interpreting the experimental results. A more thorough study of the stability of this flow, perhaps using the parabolized stability equations or direct numerical simulation, is needed.

Results

Hot-film data were obtained at two axial stations on the cone: $x/L = 0.47$ and 0.8, which correspond to local Reynolds numbers of $Re_x = 0.93 \times 10^6$ and 1.6×10^6, respectively. Data were taken for different circumferential locations at the wall-normal position where the maximum broadband rms signal was recorded. The measurement stations were chosen to meet two competing requirements. Relatively low disturbance levels were desired to ensure that the local flow condition corresponded to the linear stability regime, and a relatively high signal level was needed to obtain a good signal-to-noise ratio. Heat-transfer measurements[10] indicate that laminar flow prevailed in the range 30 deg $\leq \theta \leq$ 90 deg for $Re_x = 0.93 \times 10^6$ and in the range 45 deg $\leq \theta \leq$ 90 deg for $Re_x = 1.6 \times 10^6$ under cold wall conditions ($T_w/T_0 = 0.42$). A somewhat different range may occur for the adiabatic wall conditions under which the hot-film measurements were made. Only a relatively poor signal-to-noise ratio could be obtained in the laminar-flow region for the lower-Reynolds-number case, so that the bulk of the measurements were made at $x/L = 0.8$.

Basic Results

Power spectra derived from the hot-film signals can reveal frequency bands with high integrated disturbance growth. The results from Probe LAT are shown in Fig. 3 for selected stations around the circumference of the cone at $x/L = 0.8$. At the leading edge of the cone ($\theta = 90$ deg), a spectral peak is evident near 10 kHz, with a smaller local maximum around 70 kHz. Proceeding around the circumference from the leading edge toward the top centerline, we see that both peaks retain their identity, with slight shifts in frequency. Initially, the amplitude of the low-frequency peak grows, whereas the high-frequency peak stays about the same. The trend reverses from $\theta = 58$ deg to the top centerline ($\theta = 0$ deg), with the high-frequency component dominating the spectrum near the top centerline. For $\theta \leq 50$ deg a broadband distribution of energy in the autospectra, the presence of local maxima in the heat transfer data,[10] and disturbances visible in schlieren photographs[10] indicate that the boundary layer is transitional.

Figure 4 shows the frequencies corresponding to maxima in the power spectra (where these are distinct) for different stations around the cone at $x/L = 0.8$. The characteristic frequencies lie in the range of 60–80 kHz for the high-frequency peak and 10–20 kHz for the low-frequency peak. Also shown on the plot are the frequencies corresponding to the largest N factor in the linear stability computation. Because of the coarse frequency resolution of the stability computations, only a rough comparison of theory to experiment is possible. Nevertheless, in the range of stations where unstable laminar flow prevailed (50 deg $\leq \theta \leq$ 90 deg), the low-frequency spectral peak seems to be captured by the linear stability computation within the available computational resolution and experimental scatter. Despite the transitional character of the region $\theta \leq 50$ deg, there is rough agreement between the high-frequency peak and the characteristic second-mode frequency.

Figure 5 shows the basic spectral results for $\theta = 45$ deg and $x/L = 0.47$, the lower-Reynolds-number case for which the best

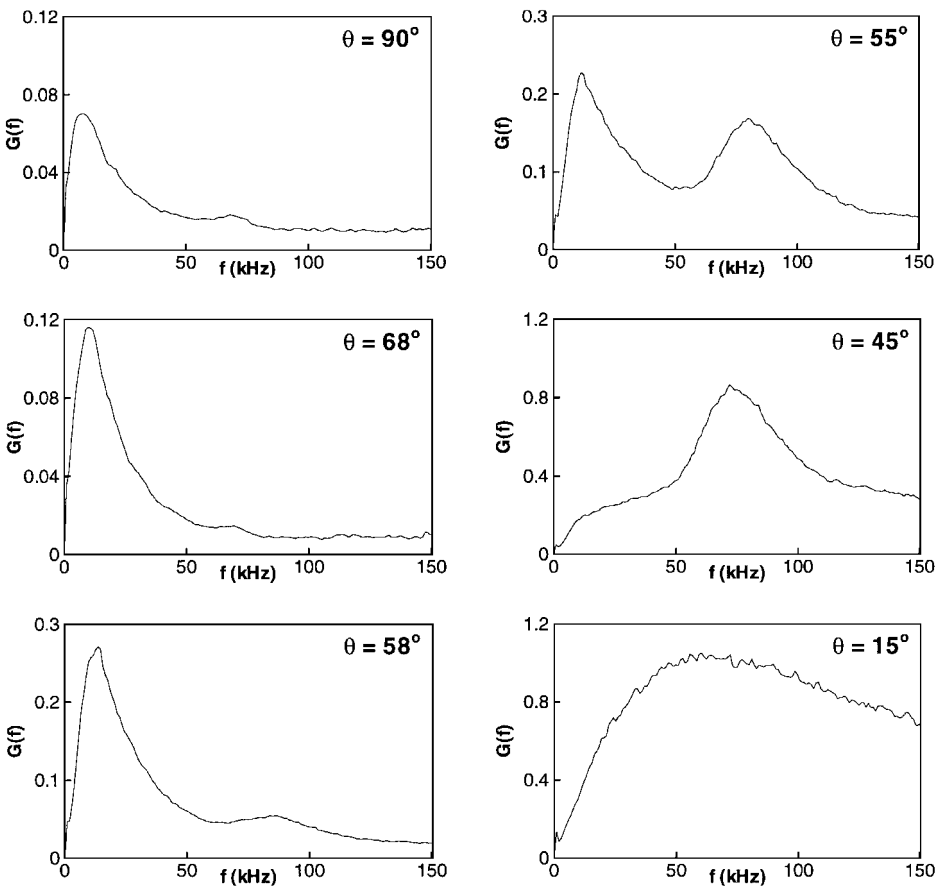

Fig. 3 Power spectra (Probe LAT) for selected stations around the circumference of the cone at $x/L = 0.8$.

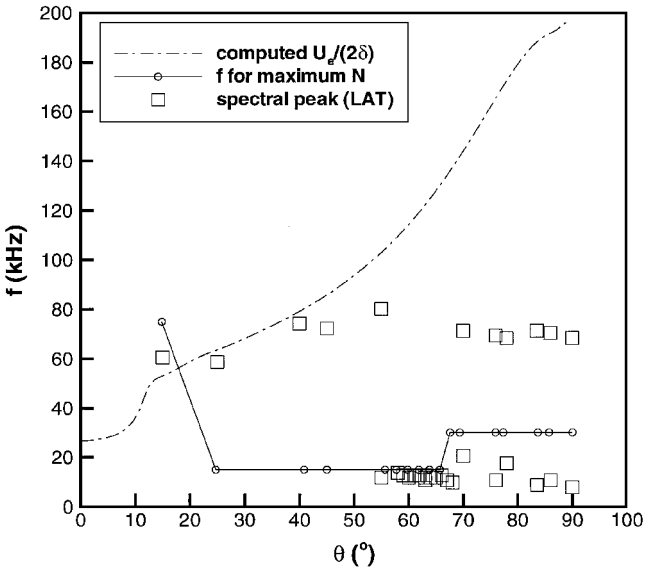

Fig. 4 Characteristic frequencies around the cone at $x/L = 0.8$.

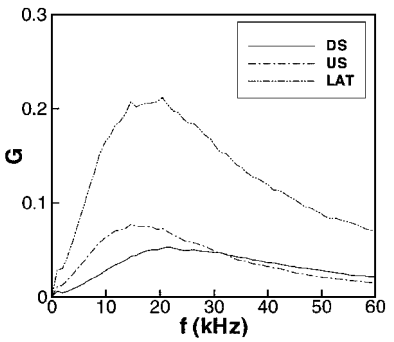

a) Autospectrum

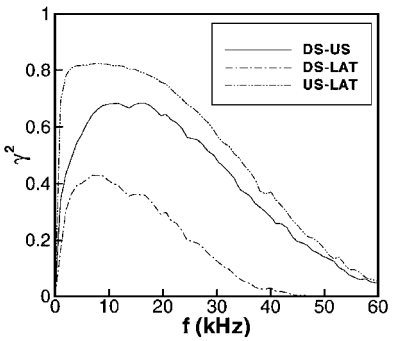

b) Coherence between each pair of probes

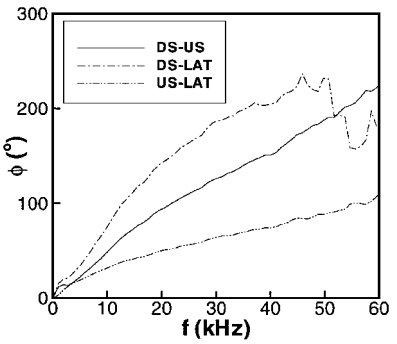

c) Phase of cross spectrum for each pair of probes

Fig. 5 Spectral data for $x/L = 0.47$, $\theta = 45$ deg.

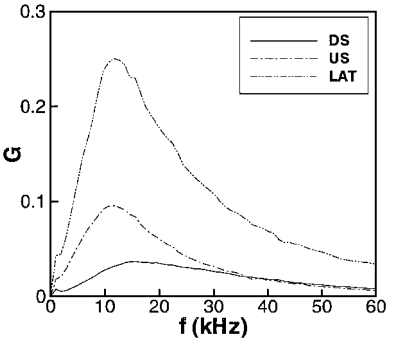

a) Autospectrum

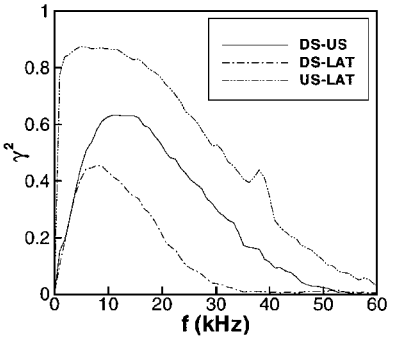

b) Coherence between each pair of probes

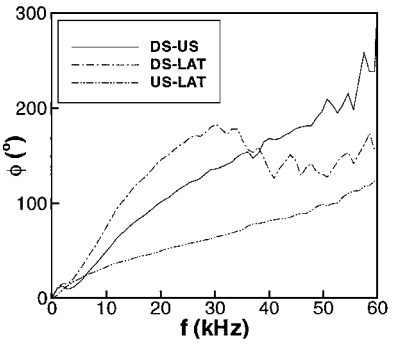

c) Phase of cross spectrum for each pair of probes

Fig. 6 Spectral data for $x/L = 0.80$, $\theta = 60$ deg.

signal-to-noiseratio was obtained. The power spectra from all three probes (Fig. 5a) show a maximum between 15 and 20 kHz, in rough correspondence with the maximum $\exp N(f)$ computed for this station. A relatively broad maximum in the coherence between the probe signals occurs between 5 and 20 kHz (Fig. 5b). The corresponding phase plots are shown in Fig. 5c.

A representative station for the higher-Reynolds-numbercase is shown in Fig. 6. The results are qualitatively the same as the preceding case. The power spectra all peak (Fig. 6a) between 10 and 20 kHz, and there is high coherence (Fig. 6b) in the 5–20-kHz range.

Instability Waves

Phase speeds corresponding to the two cases just discussed were computed according to Eq. (8) and are shown as a function of frequency in Fig. 7. In the range 10 kHz $\leq f \leq$ 30 kHz, the computed phase speeds corresponding to each pair of probes are seen to agree with a modest amount of scatter in the data. For both Reynolds numbers the phase speed varies between 300 and 400 m/s.

The wave angles corresponding to the phase speeds were computed using Eq. (7), and the results are shown in Fig. 8. The angles are measured relative to the ξ axis, which is the projection of the x axis onto a plane tangent to the cone's surface, and a positive angle indicates a direction away from the top centerline (see Fig. 2). As with the phase speeds, the phase angles computed from the three possible combinations of probes agree in the range 10 kHz $\leq f \leq$ 30 kHz, with a moderate amount of scatter. The instability waves are skewed

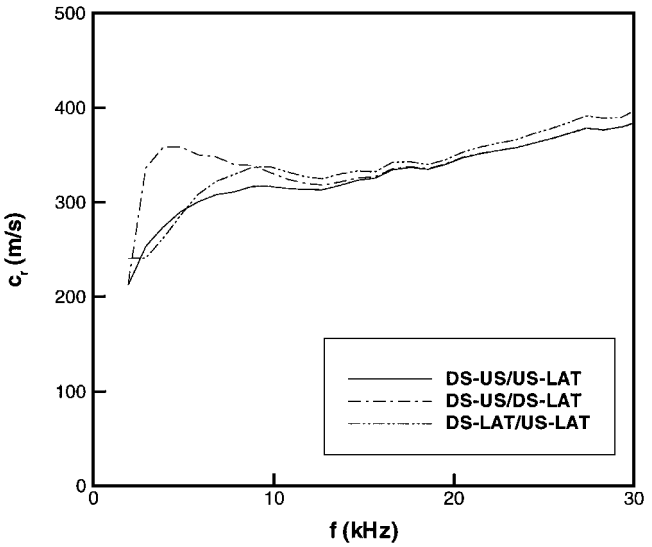

Low-Reynolds-number case: $U_e = 1131$ m/s, $x/L = 0.47$, $\theta = 45$ deg

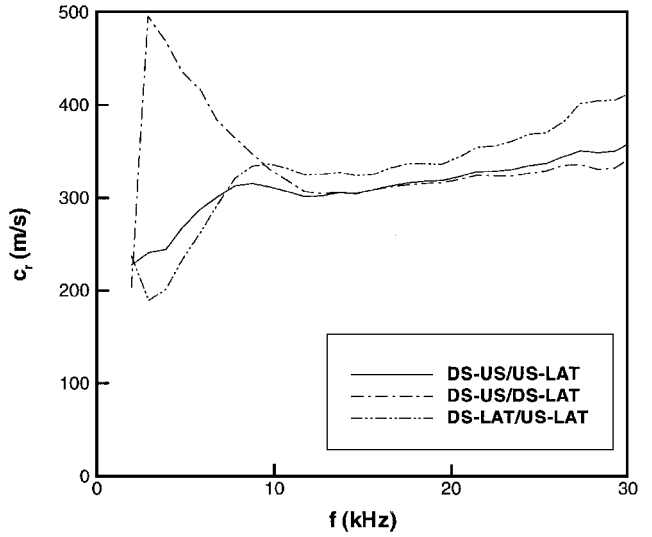

High-Reynolds-number case: $U_e = 1125$ m/s, $x/L = 0.80$, $\theta = 60$ deg

Fig. 7 Phase velocity.

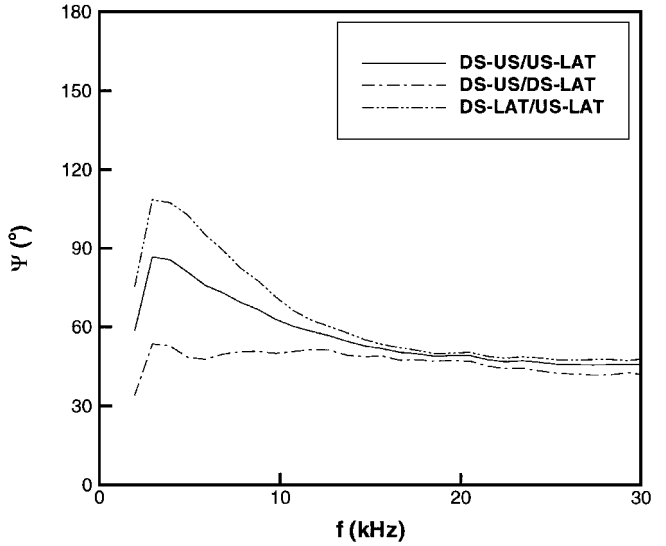

Low-Reynolds-number case: $x/L = 0.47$, $\theta = 45$ deg

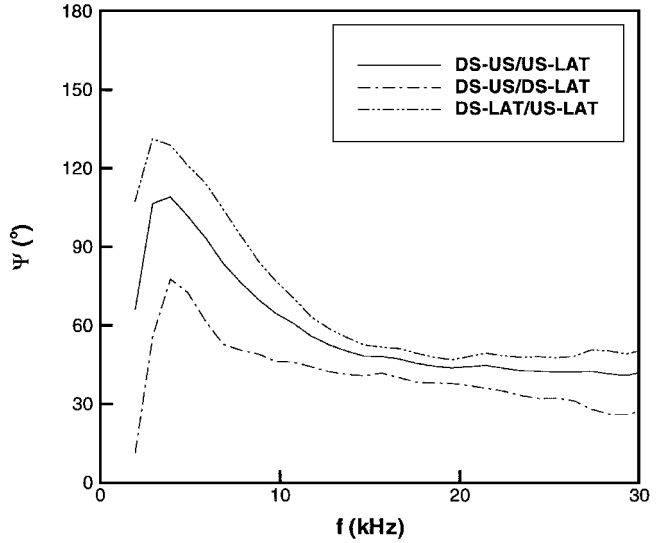

High-Reynolds-number case: $x/L = 0.80$, $\theta = 60$ deg

Fig. 8 Angle corresponding to phase velocity.

from the freestream flow direction, as expected for a crossflow instability. Here we see 45 deg $\leq \Psi \leq$ 60 deg, whereas the angle of the boundary-layer-edge streamlines from the ξ direction is at most 10 deg in this portion of the flow.

The phase velocity is shown as a function of circumferential station around the cone in Fig. 9, for $f = 14.6$ kHz and $Re_x = 1.6 \times 10^6$. The frequency was chosen to be as close as possible to the frequency with the maximum computed amplification rate, and the range of circumferential stations shown corresponds to the best signal-to-noise ratio obtained for the laminar-flow regime. The experimental values for the three possible probe combinations are compared to the value predicted by the linear stability computation for $f = 15$ kHz. The freestream velocity distribution is included for reference. The experimental phase velocity is in the range 300–400 m/s, whereas theory predicts a phase velocity of 175–250 m/s over the same range of stations. (The rapid changes in the theoretical curve for $\theta \leq 15$ deg reflect switches in the most-amplified instability mode. The rapid variation in boundary-layer thickness in this region of the flow[10] and the presence of several unstable modes with similar amplification rates may lead to inaccuracies in the linear stability analysis for this range of circumferential stations. This problem should not significantly affect the results away from the top centerline of the cone.)

Because we are considering a fixed frequency, the wavelength plot (Fig. 10) has the same form as the phase-velocity plot. The wavelength predicted by linear stability theory follows the same trend

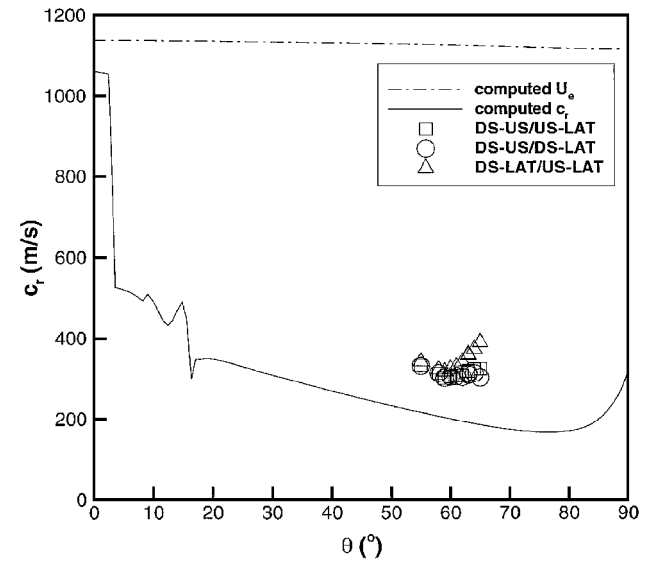

Fig. 9 Phase velocity vs circumferential station at $x/L = 0.80$.

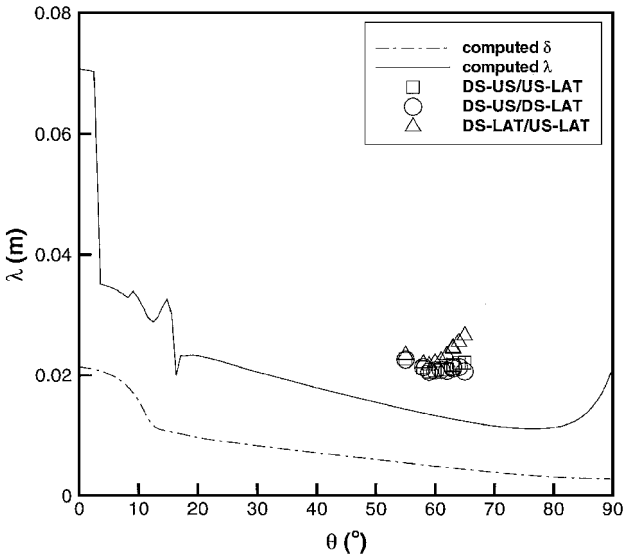

Fig. 10 Wavelength vs circumferential station at $x/L = 0.80$.

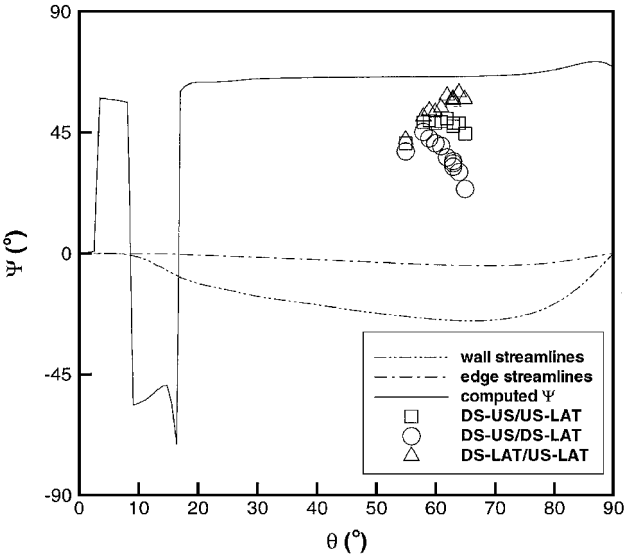

Fig. 11 Wave angle vs circumferential station at $x/L = 0.80$.

as the boundary-layer thickness over much of the cone's circumference. The computation predicts wavelengths in the range of about 15–25 mm (about 2.5δ), and the experimental values are between 20 and 30 mm.

Figure 11 shows measured and computed wave angles; the angles of the edge and wall streamlines are included for reference. All of the angles are measured from the ξ axis, and a positive angle indicates an orientation outboard of the top centerline of the cone. The computation predicts wave angles in the range 60–70 deg, whereas the experimental wave angles are in the range of 30–60 deg. Despite the scatter in the data, the results suggest wave propagation in a direction significantly skewed from the edge velocity vector.

The relatively large scatter in the wave angles may have a number of causes. A differential error analysis of Eqs. (7) and (8) gives, for example, $\Psi = 48 \pm 12$ deg and $c_r = 304 \pm 24$ m/s for the case DS-US/US-LAT, $f = 14.6$ kHz, $\theta = 60$ deg, and $x/L = 0.8$, assuming errors in the time delays of 1 μs. This is about the level of scatter in the plots. Other potential sources of error, such as mismatch between probes in y/δ location, differences in probe sensitivity, and probe interference effects, are more difficult to quantify.

Conclusions

Simultaneous measurements were carried out with three hot-film probes in the three-dimensional boundary-layer flow over an elliptic cone of 2:1 aspect ratio at Mach 8, and the data obtained were compared to the results of computations using the parabolized Navier–Stokes equations and linear stability theory. The elliptic-cone flow was found to be significantly different from the flows studied in previous hypersonic-flow stability experiments, which have focused exclusively on wind-tunnel models with two-dimensional, axial or planar symmetry. At least two instability mechanisms appear to be active in the present flow: one associated with the region of maximum crossflow in the vicinity of the shoulder of the cone and the other associated with the inflectional velocity profiles on the top centerline. N-factor contours were double lobed, with one lobe associated with each of these two regions of the flow (see Fig. 15 of Ref. 9).

In the vicinity of $\theta = 60$ deg at $x/L = 0.8$, the dominant instability had a characteristic frequency between 10 and 20 kHz. For frequencies in this range, instability waves in the elliptic-cone flow had a wavelength of roughly 4δ and traveled at a phase speed of approximately $c_r/U_e = 0.3$, skewed outboard about 45 deg from the edge streamlines. Rough agreement was found between the linear stability computation and the experimental results.

There does not appear to be an easy, decisive test to identify whether low-frequency traveling waves represent crossflow or first-mode instability. A straightforward approach would be to examine the disturbance velocity field for evidence of crossflow vortices, but we have not been able to identify features in our computations that can be unambiguously identified as crossflow vortices. Malik and Balukumar[4] note that amplification rates and wave angles increase continuously with increasing boundary-layer crossflow but that the disturbance wavelength is distinctly shorter at low frequency for a crossflow instability than for a first-mode instability. The relatively short wavelengths found in the present study do suggest a crossflow instability according to this criterion.

The flow in the vicinity of the top centerline of the cone, where the velocity profiles were inflectional, was found to be highly unstable. Power spectra obtained in this region of the flow showed a peak at relatively higher frequency (60–80 kHz), which agreed with the characteristic second-mode frequency ($U_e/2\delta$) for circumferential stations on the upper part of the cone ($\theta \leq 50$ deg) for $Re_x = 1.6 \times 10^6$. Similar unstable frequencies were obtained in the linear stability computations, but comparison between theory and experiment in this region of the flow must be made with caution because the flow in the experiment appeared to be transitional for $\theta \leq 50$ deg.

The flow in the vicinity of the leading edge was found to be relatively stable, as compared to other stations around the circumference, but spectral peaks of low amplitude were observed experimentally in this region. Linear stability computations showed small amplification rates and small integrated disturbance amplitude on the leading edge. The direction of the group-velocity vector was never more than about 1 deg from that of the edge-velocity vector for all stations around the circumference of the cone at $x/L = 0.8$, which suggests that disturbances initiated off the leading edge do not contribute significantly to the amplitude at the leading edge in the computations. The peaks seen in the experiments may be caused by spreading of disturbance energy by a mechanism not included in the linear stability model; more sophisticated modeling could resolve this issue.

The present study has demonstrated a case in which crossflow has a significant influence on transition in a three-dimensional configuration, under conditions that would lead to second-mode dominated transition in a similar two-dimensional configuration. The qualitative differences between the two- and three-dimensional cases are interesting from a scientific perspective and must be considered in engineering prediction of transition because significant regions of crossflow and three-dimensionality tend to be present in the boundary-layer flow over actual aerospace vehicles.

Additional work is warranted to overcome the experimental limitations of wind-tunnel noise and instrument sensitivity. In particular, detailed measurements of wave orientation and disturbance growth rates could help to confirm the identity of the instability modes present in the flow. Further, the parallel-flow assumption used in the present linear stability computations is not expected to be a good approximation for regions of the flow with a high degree of three-dimensionality. More complex mathematical models, such as the

parabolized stability equations, the linearized Navier–Stokes equations, or the full Navier–Stokes equations, could yield additional insight into the physics of this interesting flow.

Acknowledgments

This project was sponsored by the U.S. Air Force Office of Scientific Research and monitored by L. Sakell and S. Walker. J. Donaldson, C. Nelson, A. Davenport, and co-workers at Sverdrup Technology, Inc., supported the experimental component of this project, and A. Demetriades of Montana State University supplied the hot-film probes. A. Creese provided assistance in the preparation of this paper. We would also like to acknowledge helpful discussions with M. Malik of High Technology Corporation on how to distinguish a crossflow instability from a first-mode instability. Cross spectra presented in an earlier conference paper on this project (AIAA 98-0435) contained an error that has been corrected in the present paper.

References

[1]Mack, L. M., "Linear Stability Theory and the Problem of Supersonic Boundary Layer Transition," *AIAA Journal*, Vol. 13, No. 3, 1975, pp. 278–289.

[2]Mack, L. M., "Boundary-Layer Linear Stability Theory," *Special Course on Stability and Transition of Laminar Flow*, R-709, AGARD, 1984, pp. 3-1–3-81.

[3]Mack, L. M., "On the Inviscid Acoustic-Mode Instability of Supersonic Shear Flows, Part 1: Two-Dimensional Waves," *Theoretical and Computational Fluid Dynamics*, Vol. 2, No. 1, 1990, pp. 97–123.

[4]Malik, M., and Balakumar, P., "Instability and Transition in Three-Dimensional Supersonic Boundary Layers," AIAA Paper 92-5049, Dec. 1992.

[5]Balakumar, P., and Reed, H. L., "Stability of Three-Dimensional Supersonic Boundary Layers," *Physics of Fluids A*, Vol. 3, No. 4, 1991, pp. 617–632.

[6]Reed, H. L., and Saric, W. S., "Stability of Three-Dimensional Boundary Layers," *Annual Review of Fluid Mechanics*, Vol. 21, 1989, pp. 235–284.

[7]Stetson, K. F., Thompson, E. R., Donaldson, J. C., and Siler, L. G., "Laminar Boundary Layer Stability Experiments on a Cone at Mach 8, Part 3: Sharp Cone at Angle of Attack," AIAA Paper 85-0492, Jan. 1985.

[8]Doggett, G. P., Chokani, N., and Wilkinson, S. P., "Effect of Angle of Attack on Hypersonic Boundary Layer Stability," *AIAA Journal*, Vol. 35, No. 3, 1997, pp. 464–470.

[9]Kimmel, R. L., Klein, M. A., and Schwoerke, S. N., "Three-Dimensional Hypersonic Laminar Boundary-Layer Computations for Transition Experiment Design," *Journal of Spacecraft and Rockets*, Vol. 34, No. 4, 1997, pp. 409–415.

[10]Kimmel, R. L., Poggie, J., and Schwoerke, S. N., "Laminar-Turbulent Transition in a Mach 8 Elliptic Cone Flow," *AIAA Journal*, Vol. 37, No. 9, 1999, pp. 1080–1087.

[11]Donaldson, J. C., and Coulter, S. M., "A Review of Free-Stream Flow Fluctuation and Steady-State Flow Quality Measurements in the AEDC/VKF Supersonic Tunnel A and Hypersonic Tunnel B," AIAA Paper 95-6137, April 1995.

[12]Kimmel, R. L., and Poggie, J., "Disturbance Evolution and Breakdown to Turbulence in a Hypersonic Boundary Layer: Ensemble-Averaged Structure," AIAA Paper 97-0555, Jan. 1997.

[13]Bendat, J. S., and Piersol, A. G., *Engineering Applications of Correlation and Spectral Analysis*, Wiley-Interscience, New York, 1980.

[14]Kimmel, R. L., Demetriades, A., and Donaldson, J. C., "Space-Time Correlation Measurements in a Hypersonic Transitional Boundary Layer," *AIAA Journal*, Vol. 34, No. 12, 1996, pp. 2484–2489.

[15]Bendat, J. S., and Piersol, A. G., *Random Data: Analysis and Measurement Procedures*, 2nd ed., Wiley, New York, 1986.

[16]Bippes, H., and Nitschke-Kowsky, P., "Experimental Study of Instability Modes in a Three-Dimensional Boundary Layer," *AIAA Journal*, Vol. 28, No. 10, 1990, pp. 1758–1763.

[17]Deyhle, H., Höhler, G., and Bippes, H., "Experimental Investigation of Instability Wave Propagation in a Three-Dimensional Boundary-Layer Flow," *AIAA Journal*, Vol. 31, No. 4, 1993, pp. 637–645.

[18]Lawrence, S. L., Tannehill, J. C., and Chaussee, D. S., "An Upwind Algorithm for the Parabolized Navier–Stokes Equations," AIAA Paper 86-1117, May 1986.

[19]Malik, M. R., "e^{Malik}: A New Spatial Stability Analysis Program for Transition Prediction Using the e^N Method," High Technology Corp., HTC-8902, Hampton, VA, March 1989.

P. Givi
Associate Editor